RSC Advances

PAPER

View Article Online
View Journal | View Issue

Check for updates

Cite this: *RSC Adv.*, 2020, **10**, 23953

In situ formation of phosphorus-doped porous graphene *via* laser induction

Weiwei Yang, [a] Ying Liu,[a] Qiushi Li,[b] Jie Wei, [a] Xueli Li,[a] Yi Zhang[ac] and Jiping Liu*[a]

Heteroatom-doped graphene exhibits high energy storage performance when used as an active electrode, and which can been applied to various advanced applications, but challenging in synthesis, *e.g.*, hazardous chemical reagents usage, difficult processing steps, and energy consumption. We demonstrated a ready, rapid and normal method for generating phosphorus-doped graphene (LIPG) using a CO_2 laser on polyimide (PI) substrate mixed with ammonium polyphosphate (APP) in ambient air. LIPG was approved and successfully synthesized *via* TEM, SEM, XRD and Raman observations. Moreover, we discussed the flame-retardant performance of APP for synthesizing LIPG on PI substrates, increasing the degree of graphitization. Furthermore, LIPG prepared using supercapacitors as an electrode showed good electrochemical performance. Remarkably, the highest specific capacitance of porous LIPG is about 206 F g^{-1} at the current density of 0.025 A g^{-1}, the value is about 2 times higher than those undoped laser induced graphene (LIG). Such great performance of the LIPG electrode material is attributed to the formation of a hierarchical porous structure, phosphorus atom doping, and manufacturing deficiency. Hence, LIPG showed considerable potential in the electrochemical application field. The proposed preparation of LIPG is best suited for synthesis and applicable to the doping of other heteroatoms doped into graphene.

Received 15th April 2020
Accepted 9th June 2020

DOI: 10.1039/d0ra03363d

rsc.li/rsc-advances

Open Access Article. Published on 23 June 2020. Downloaded on 1/23/2026 11:39:11 PM.
This article is licensed under a Creative Commons Attribution-NonCommercial 3.0 Unported Licence.

1 Introduction

Graphene has attracted considerable attention due to its invincible physical, chemical, mechanical, and electrical performance[1–4] and is reported to have broad application prospects in energy storage,[5,6] electronics,[7] electrocatalysis[8,9] and sensors.[10,11] Compared with pristine graphene, the doping of heteroatoms, such as P, N, or B, into graphene results in an ordered bandgap and changes in electronic and electrochemical performances, which affords electrochemically active sites and broadens the scope of application.[12–16] These hybrid graphene materials possess high specific area, thermal and electrical conductivity, and can become dream candidates for a new generation of sorbents, photo-catalysts, electrodes, sensors, biosensors, antibacterial materials, surface treatments, and multi-function membranes.[17–19] Furthermore, atom doping has a potential application in catalysis/electrocatalysis field. Qiu *et al.*[20] studied Co-doped graphene and applied it as a rechargeable Zn–air battery, which shows high performance. As such, the catalytic performance may be interesting to promote the study of atom-doped graphene, which has attracted attention from researchers. Moreover, Qiu *et al.*[21] had investigated that N-doped graphene can significantly improve electrochemical performance, and therefore atom-doped graphene is a very meaningful study. However, these traditional preparation methods of heteroatom-doped graphene are confronted with the challenge of a redundant process of the synthesis of graphene oxide, the deposition of nanoparticles, and the reduction of graphene oxide.[22–24] Thus, hunting for a new method to prepare atom-doped materials with low cost, easy processing, and high-energy storage performance is urgently required.

Porous 3D graphene synthesized *via* a facile and simple laser induction (LIG) has recently attracted considerable attention.[25–27] The LIG method is a convenient, highly efficient, low cost and environmentally friendly potential candidate for synthesizing heteroatom-doped graphene. Ye[28] attempted a trial doping of Co, Mo, and Fe into LIG, which had high electrochemical performance and is applied as an energy storage device. However, a high-pressure film forming process is required during the preparation process, which complicated the preparation, therefore, this process needs to be improved. L. *et al.*[29] prepared N-doped LIG using reduced graphene oxide (GO) by a femtosecond laser direct writing method under an ammonia atmosphere. It showed great application for flexible fabrication and graphene-based devices; however, the as-

[a]*School of Materials Science and Engineering, Beijing Institute of Technology, Beijing 100081, China. E-mail: liujp@bit.edu.cn*

[b]*CAS Key Laboratory of Space Manufacturing Technology, Technology and Engineering Center for Space Utilization, Chinese Academy of Sciences, Beijing 100094, China*

[c]*Department of Biology and Chemical Engineering, Shandong Vocational College of Science & Technology, Weifang 261053, China*

Open Access Article. Published on 23 June 2020. Downloaded on 1/23/2026 11:39:11 PM.
This article is licensed under a Creative Commons Attribution-NonCommercial 3.0 Unported Licence.

prepared graphene had almost no hierarchically connected pores and the laser equipment increased the cost. Wang *et al.*[30] successfully produced high electrochemical performance LIG doped with N atom (LING), whereas the auxiliary essential GO increased both cost and process difficulty. Accordingly, an inexpensive and simple method to prepare hierarchically porous heteroatom-doped graphene with high performance has become important.

Generally, non-metallic heteroatoms such as N, S, P, and B, are usually selected for doping to enhance the electrochemical performance of graphene.[31] Among these, graphene doped with P atoms is more stable under a positive potential and shows high specific capacitance; thus, it widens the potential window and enhances the energy storage capacity of the graphene material.[32,33] Consequently, hierarchically porous laser-induced phosphorus-doped graphene possesses enormous potential in the energy field. Due to its special structure and performance, LIPG can be potentially applied in the catalysis/electrocatalysis field. However, the laser-induced high-performance hierarchically porous LIPG has not been reported to date. Ammonium polyphosphate (APP), a highly effective and inexpensive flame retardant, could be converted into phosphate at high temperatures. Moreover, APP acts as both a retardant and P supplier for laser induction processing, thus providing an opportunity for synthesizing phosphorus-doped LIG.

Combined with the most commonly used polymer LIG substrate polyimide (PI),[34] herein, in this work, we demonstrated a one-step method to selectively generate phosphorus-doped hierarchically porous graphene *via* 10.6 μm CO_2 laser-induction (LIPG), innovatively using APP as the retardant and P as the supplier. Compared with other LIGs, LIPG significantly improved electrochemical performance due to the graphitization aroused by the flame retardant properties of APP. Furthermore, we applied LIPG to fabricate supercapacitors that showed high conductivity, indicating the great application potential of LIPG. The synthesis strategy is extremely facile, rapid, inexpensive and versatile, thus providing a prospective approach for LIPG production and performance improvement.

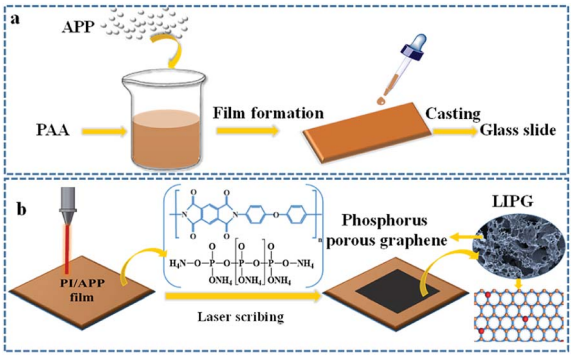

Fig. 1 Schematic of the formation of LIPG from the PI/APP film. (a) Preparation of the PI/APP film from PAA containing the APP solution; (b) LIPG fabricated on PI/APP film by laser induction.

2 Experimental

2.1 Preparation of PI/APP film

Polyimide solution (PAA) was purchased from Changzhou Friend Plastic New Material Co., Ltd., and ammonium polyphosphate (APP: $n > 2000$) was purchased from Qingyuan Pusaifurop Chemical Co., LTD. As shown in Fig. 1a, the PAA solution is poured into a beaker, *N*-methyl-2-pyrrolidone (NMP) is added for dilatation at a ratio of 4 : 1, and then 2 wt% of APP is added to the PAA solution, followed by stirring at high speed for ~20 min (~1000 γ/min) until a homogeneous mixture is formed. Subsequently, a certain mass of the mixture is evenly dropped on a glass slide with a dropper (slide size: 25.4 × 76.2 mm^2). Ensure that the thickness of the prepared PI/APP film is consistent. Removing the NMP solvent in a vacuum drying oven as the following curing process, then the PAA solution was converted into a brown PI film. The curing process is as follows: 80 °C/20 min + 120 °C/20 min + 160 °C/30 min + 180 °C/20 min + 200 °C/20 min + 220 °C/20 min + 250 °C/20 min + 300 °C/10 min. Using the abovementioned process, the PI film shows good mechanical properties. We then placed the slide in deionized water and removed the PI film.

2.2 LIPG fabricated on PI/APP

Laser scribing on the PI/APP film was conducted on a 4060 non-metal engraving machine equipped with a CO_2 pulsed laser (10.6 μm, 50 W) (spot diameter 0.001; power 1–100% adjustable, engraving speed 1–100% adjustable). Fig. 1b shows that after inducing the PI/APP composite film *via* a CO_2 infrared laser in air, the radiation part of the PI/APP film was converted into a porous phosphorus-doped graphene (LIPG). Compared with this method of preparing graphene, traditional chemical vapour deposition progress has several disadvantages, for instance, high drying temperature,[35] post-processing and requiring tedious stepwise, such as etching, critical drying point, and aerogel formation.[36,37] The surface of the PI/APP film can be readily and briefly converted into LIPG due to its aromatic structure, and the pattern on the film can be designed by controlling the computer (Fig. 1b). The different laser parameters have a significant effect on the graphitization degree of LIPG (Fig. 4b). In this work, LIPG was formed when the laser power is 5–9 W and the laser speed was 100 mm s^{-1}. When increasing the laser power and laser speed, it will result in the ablation of PI/APP and no LIPG will be obtained.

2.3 Device fabrication

The impurities and surface oxide layer were removed by cleaning the Ni foam substrate with isopropyl alcohol. Preparing the mixed solution with 1 ml ethanol solution and 5 mg PTFE solution, followed by ultrasonic dispersion for 10 min. The conductive substance deposited on the surface of the Ni foam consists of 4 mg of LIPG and 0.5 mg of conductive graphite, then add to the prepared mixed solution and shake evenly, then ultrasonically disperse for 20 minutes, use a disposable pipette to draw a small amount of the mixture (~170 μl) and add it to the smooth surface of the foamed nickel. It is preferable to form

 This journal is © The Royal Society of Chemistry 2020

Open Access Article. Published on 23 June 2020. Downloaded on 1/23/2026 11:39:11 PM.
This article is licensed under a Creative Commons Attribution-NonCommercial 3.0 Unported Licence.

a flat droplet by dropping and completely covering the smooth surface of the Ni foam. The prepared electrode is then placed in a vacuum drying oven and dried at 80 °C for 12 h. The proportion of each component is active material : conductive carbon black : PTFE = 80 : 10 : 10. The dried electrode is weighed, and the quality of the active conducting component is calculated and recorded, which is preferably 1–2 mg.

2.4 General characterization

The surface morphologies and structures of materials were characterized using SEM (JSM-IT300). TEM images were obtained using the machine FEI Tecnai G2 F30. Raman spectra curves were analysed with a Micro Raman imaging spectrometer (DXRxi), and the wavelength of laser excitation was 532 nm. XRD was performed on a Japan equipment (Rigaku D/Max-Ra), λ = 1.54 Å. XPS spectra curves were recorded using an X-ray photoelectron spectrometer Al Kα radiation (AXIS Supra). The LIPG powders were obtained from the surface of LIPG films and used for TEM, XRD, and XPS analyses. Other general characterizations data were directly obtained from the LIPG film surface.

Figuring out the crystalline size by using Raman spectroscopic data, crystalline size in the axis (L_a) was obtained by eqn (1)[38] from the peak value ratio of the G peak (I_G) and D peak (I_D).

$$L_a = \left(2.4 \times 10^{-10}\right) \times \lambda_l^4 \times \left(\frac{I_G}{I_D}\right) \quad (1)$$

In the equation, λ_l represents the wavelength of the Raman laser (λ_l = 532 nm).

2.5 Electrochemical characterization of LIPG

The electrochemical behaviours of all the prepared LIPG devices are identified in a three-electrode equipped using the CHI 660 workstation machine. A Pt plate and Hg/HgO (in 3 M KOH) were applied as the reference and counter electrode, respectively. Moreover, all the electrochemical tests were performed in a 1 M KOH solution.

Fabrication of supercapacitor application device: print the circuit using a CO_2 laser on the PI/APP film, solidify the copper wire using a silver paste (80 °Cfor 30 min), connect one end of the LED small bulb with a copper wire, and connect the other copper wire to the Keysight end. Then, connect one end to Keysight to obtain a device that demonstrates the conductivity of LIPG.

2.6 Calculation for the electrochemical performance of LIPG supercapacitor

The specific capacitances (C_{sc}, F g^{-1}) according to the GCD curves were reported using eqn (2):[39]

$$C_{sc} = \frac{I\Delta t}{m\Delta U} \quad (2)$$

where I is the discharge current, m is the mass of the active electrodes, Δt is the discharge time, and ΔU is the operating voltage window.

3 Results and discussion

The surface morphology of LIPG was investigated by SEM, and the micro and nanostructure of LIPG flakes were investigated by TEM. As shown in Fig. 2a depicts, the surface of PI/APP film irradiation by a CO_2 infrared laser (10.6 μm) in the air atmosphere converts the PI/APP film into phosphorus-doped graphene (LIPG). Note that under the induction of the laser, the PI/APP film can be easily converted into LIPG. Interestingly, the images in Fig. 2a shows two differentiated areas: the portion of LIPG exposed to the laser (circled in Fig. 1a) and the smooth part that was unexposed. Fig. 2b shows the images in Fig. 2a; the image shows the surface of LIPG formed on PI/APP film. Fig. 2b shows that a porous structure is formed orderly along the scanning trace of the laser from up and down. The porous-like morphology on the surface of the LIPG film is due to the release of gas. From the high-magnification image, the hierarchical porous graphene structure becomes more distinctive (Fig. 2c). These porous structures increase the specific areas and promote electrolyte penetration into the active electrode materials.

To study the surface structure of LIPG, the LIPG mixed suspension was dropped onto a carbon grid to analyse the TEM images. Fig. 2d shows the structure of LIPG with few layers. As shown by the HRTEM images, a large number of ripple-like wrinkled structures can be identified on the surface of LIPG (Fig. 2e and f). The edges of LIPG flakes consist of few-layer (<10 layers). In Fig. 2e, these ripple-liked structures of LIPG flakes can be seen, which can increase the electrochemical performance of electrode devices.[40] The layers of LIPG in Fig. 2f tested by high-resolution TEM image shows the nano shaped ripples, which are revealed at the edges of LIPG and less than 10 layers. The formation of these corrugated structures is attributed to the surface thermal expansion generated by laser radiation. The

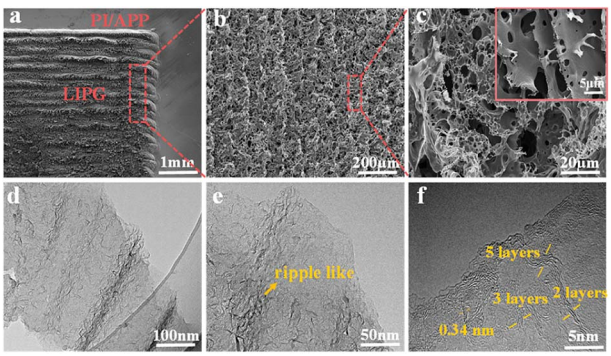

Fig. 2 The SEM and TEM images of LIPG formed on PI/APP. (a) Cross-sectional SEM image of the LIPG film on the PI/APP film, scale bar, 1 mm, (b) SEM image of the LIPG film circled in (a) scale bar, 200 μm, (b) high multiples image of the LIPG film circled in; (c) scale bar, 20 μm; the images insert (c) scale bar, 5 μm; (d) TEM images of LIPG formed on PI/APP, (e) high-resolution TEM (HRTEM) image taken at the edge of a LIPG flake showing ripple-like structures; scale bar, 50 nm, (f) HRTEM image of LIPG showing few-layer features and average lattice space of 0.34 nm corresponds to the (002) planes of graphitic materials; scale bar, 5 nm.

Open Access Article. Published on 23 June 2020. Downloaded on 1/23/2026 11:39:11 PM.
This article is licensed under a Creative Commons Attribution-NonCommercial 3.0 Unported Licence.

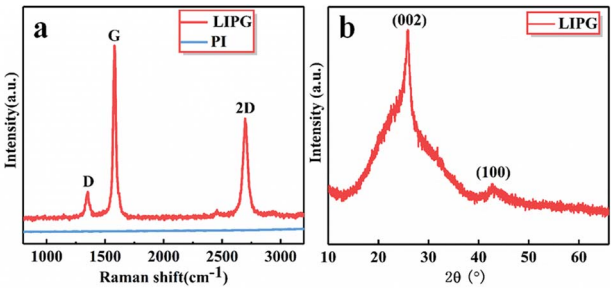

Fig. 3 Characterizations of LIPG prepared by laser on PI/APP film. (a) Raman spectrum of LIPG and PI; (b) XRD of powdered scraped from LIPG.

average lattice space tested by the computer software is about B3.4 Å (Fig. 2f), which corresponds to space between two adjacent (002) planes in graphitic materials, and the consequence are well-matched with the XRD analysis (Fig. 3b).

The existence of graphene is confirmed by Raman spectra (Fig. 3a). The Raman spectrum shows three peaks: D, G and 2D, which were all list in the manuscript, G peak near 1580 cm^{-1} and a 2D peak at ~2700 cm^{-1}, which is generated from the second-order zone-boundary phonons. For graphene samples containing defects or at the edges of graphene, there is also a defect D peak at around 1350 cm^{-1}. The 2D peak and G peak readily verifies graphene-based material, which can be matched with the Lorentzian peak centered at the location of 2700 cm^{-1}, which is the same as layer graphene. This 2D band profile shown in Fig. 3a is typical of that observed in 2D graphite materials: randomly stacked graphene flake layers along the *c* axis. The D band represents suggestive of graphene sheets structures or other defects sites. The degree of graphitization can be indicated by the I_G/I_D value, and we calculated the I_G/I_D value using eqn (1). The X-ray diffraction (XRD) curves of LIPG on PI/APP film shows peaks at 25.9°, which is attributed to the (002) plane, and another peak at 42.9° (2θ), which is attributed to the (100) plane (Fig. 3b). The interlayer distance (Ic) of the peak at 25.9° (2θ) is about 3.4 Å, thus indicating a relatively high level of graphitization, as well as another peak at 42.9°, corresponding to the in-plane structure. The characteristics of the XRD curve agreed with the characteristics of graphene.

The effect of laser technology parameters on fabricating LIPG has been investigated by changing the laser power. Several LIPG samples were prepared for Raman test using a laser power ranging from 5 to 9 W, and the scan rate was 100 mm s^{-1}. The degree of graphitization of carbon materials was characterized by Raman spectroscopy. In Fig. 4a, with increase in laser power, the intensity of D peak increased to a high value of 8 W, and the degree of graphitization reached the maximum value. As the laser power increased to >8 W, the graphitization degree of LIPG accordingly declined because the oxidation reaction in air or part of PI/APP ablated. The statistical analysis of I_G/I_D (peak of the I_G, I_D value) *versus* laser power provides a similar result, which can be seen in Fig. 4b. Moreover, the crystalline size (L_a) of LIPG along the *a*-axis is broken down using Raman results.[29] As shown in Fig. 4c, the L_a values reported *via* the average I_G/I_D ratio using eqn (1) shows an enhanced L_a of up to 82.37 nm at a LIPG power of 8 W. A continual increase in the laser power will lead to a decrease in the size of graphene *e.g.*, the L_a value decreased to 44.74 nm when the laser power was 9 W. This corresponding to the value I_G/I_D in Fig. 4b. Adjusting proper laser induction parameters is an available approach for adjusting the crystalline size and layers of LIPG. The degree of graphitization I_G/I_D reaches ~4.4, which is two times higher than that of LIG formed on PI films. Due to the flame retardant effect of APP on PI, the carbonization ability of PI was promoted;[41,42] therefore, the degree of graphitization improved compared with that of PI without P doping.[29]

The chemical composition of LIPG formed on PI/APP film is analysed using XPS. As shown in Fig. 5a, pure PI/APP has four ingredients: C, O, N and P. The original content of C, O, N, and P is ~59.61%, ~29.32%, ~6.39% and ~4.68%, respectively; in LIPG, the C is ~88.9%, O is ~8.65%, N is ~0.91% and P ~2.55%. Because of the formation of LIPG, the C and O atomic content significantly increased compared with that of PI/APP without laser induction. Moreover, the N and P atomic content shows a slight decrease too. These atoms would be reintegrated and discharged as gases, and the rest pf the atoms would be rearranged to generate graphitic structures. Because of the high temperature caused by laser irradiation, some P atoms form phosphate, which can promote the dehydration of substrate to yield an amorphous carbon char;[43] therefore, the content of P decreases, and the remaining atoms combine with LIG to form LIPG. Note that PI/APP is a type of flammable retardant polymer; research on laser ablation polymers began in the early 1980s.[44] Due to the complex nature of polymers, the particular mechanism that produces ablation is still a matter of debate, which p is considered to be photothermal or photochemical technology, or both.[45] Our prepared LIPG is likely

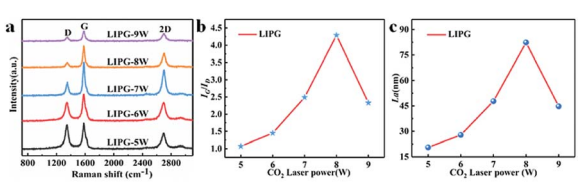

Fig. 4 (a) The Raman spectra at different laser power; (b) the integrated intensities of G and D peaks (I_G/I_D) for different LIPG; (c) the crystalline size (L_a) along the *a*-axis of different LIPG.

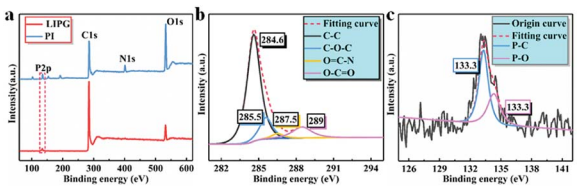

Fig. 5 The XPS curves of LIPG formed on PI/APP film. (a) An XPS survey for PI/APP film and LIPG formed on the surface of PI/APP; (b) the C 1s XPS spectrum of the LIPG prepared by laser on PI/APP; (c) the P 2p XPS spectrum of the LIPG formed on PI/APP.

This journal is © The Royal Society of Chemistry 2020

Open Access Article. Published on 23 June 2020. Downloaded on 1/23/2026 11:39:11 PM.
This article is licensed under a Creative Commons Attribution-NonCommercial 3.0 Unported Licence.

generated by photothermal effects because of the long-wavelength (~10.6 μm) of the CO_2 laser we used, that is because of photochemical processes is always exist in lasers with short wavelengths. The laser could result in extremely high temperatures (>2500 °C), and the high energy generated by laser irradiation leads to lattice vibrations. For each LIPG type, the C 1s shows C=C at 284.6 eV and C–O at 285.8 eV (Fig. 5b). The remarkable decline of oxygen and nitrogen ingredient in LIPG is attributed to the high temperature caused by laser irradiation, which could easily break the C–O, C=O and N–C bonds (Fig. 5a). The P 2p spectra curve shows two prominent peaks at ~134.2 eV and ~135.1 eV, which can be to the P–C and P–O bonds, respectively (Fig. 5c). The XPS spectrum of LIPG shows a large C atomic content, which agrees with the above-mentioned Raman and XRD analysis.

To highlight an application of LIPG formed on PI/APP, we fabricated a supercapacitor from LIPG (LG-SCs) in which LIPG electrode serves as the active electrode (marked by circles in Fig. 6a). Note that well-defined LIPG-SCs electrodes are made by LIPG powders obtained from laser induction on PI/APP. Fig. 6a shows the electrode device architecture of the prepared LIPG-SCs; the specific fabrication protocol has been reported in the Methods section (Section 2.3). Fig. 6b shows the cyclic voltammetry (CV) curves of LIPG-8 W in a potential window from 80 mV s^{-1} to 10 V s^{-1}. Notably, only one pair of redox peaks is located at ~0.28 and 0.52 V with a scan rate of 1 V s^{-1}, confirming typical pseudocapacitive characteristics of LIPG. After changing the sweep rate, all the CV curves retain similar shapes, as shown by Fig. 6c, this remarkable capacitive performance is further verified by the GCD test patterns at varying current densities range from 0.025 to 0.6 A g^{-1}. And calculate the specific capacitance (SCs) through the GCD curves with eqn (2) (Fig. 6d), the highest specific capacitance is 206 F g^{-1}, which is higher than LIPG undoped hybrid atom and the values got in recently reported GO-based supercapacitors devices.[46,47] The high capacitance generated by the LIPG-SCs is possibly attributed to the abundant wrinkles and high specific area on the surface of hierarchical porous of highly conductive graphene; this structure provides facile access for the electrolyte to generate a Helmholtz layer. Therefore, this result indicates that this method inspires researchers to further develop the potential of other polymers. Fig. 6e shows various circuit shapes can be scanned directly on the surface of the LIPG, and the LED small bulb connects with LIPG, by connecting the two ends of the copper wire, the LED bulb lights up, which demonstrates the LIPG owns good conductivity. The phenomenon is agrees with the above characterization.

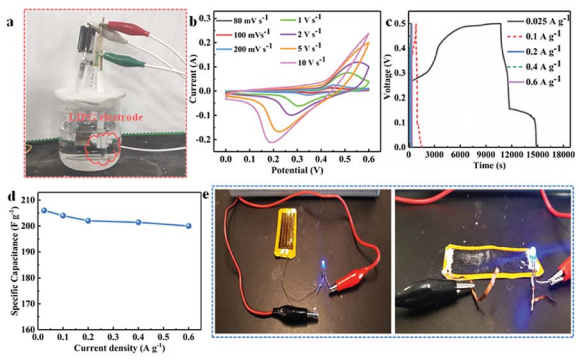

Fig. 6 (a) The LIPG-SCs device fabricated by LIPG-8 W; (b) CV curves of the LIPG-8 W electrode at the scan rate from 80 mV s^{-1} to 10 V s^{-1}; (c) GCD curves of the LIPG-8 W electrode at various current densities ranging from 0.025 to 0.6 A g^{-1}; (d) the specific capacitance of LIPG-8 W over a current density range of 0.025 and 0.6 F g^{-1}; (e) the LED lamp to connect with LIPG using a copper wire.

4 Conclusions

In this research, we demonstrated a simple and rapid method for transforming PI/APP to phosphorus porous graphene by CO_2 laser-induction with different operational modes, laser power, and laser speed. This study reported that the inherent aromatic structure of PI and the flame retardant APP effect on the material is important to the degree of graphitization of LIPG. Moreover, phosphorus is directly doped during laser induction, which is of great help for improving the performance of LIPG in the application. Besides, LIPG is applied to supercapacitor for further study, which shows high specific capacitance and with a maximum 206 F g^{-1}. We developed a device to demonstrate the electrical conductivity of LIPG. Accordingly, the method for generating LIPG electrodes in our work should be appropriate to the preparation of heteroatom-doped (S, P, Ni) laser-induced hierarchical porous graphene, which has significant application potential in the exploitation of advanced micro-energy storage and catalysis/electrocatalysis devices.

Conflicts of interest

There are no conflicts to declare.

Acknowledgements

This work was funded by the MJ-2016-F-11. Dr Jiping Liu thanks the foundation for support.

Notes and references

1 F. Schedin, A. K. Geim and S. V. Morozov, *Nat. Mater.*, 2007, **6**, 652–655.
2 K. S. Novoselov, V. I. Fal'ko and L. Colombo, *Nature*, 2012, **490**, 192–200.
3 A. A. Balandin, S. Ghosh, W. Z. Bao, I. Calizo, D. Teweldebrhan, F. Miao, C. N. Lau and Z. Wen, *Nano Lett.*, 2008, **8**, 902–907.
4 N. A. Kumar, H. J. Choi, Y. R. Shin, D. W. Chang, L. M. Dai and J. B. Baek, *ACS Nano*, 2012, **6**, 1715–1723.
5 X. B. Wang, Y. J. Zhang, C. Y. Zhi, X. Wang, D. M. Tang, Y. B. Xu, Q. H. Weng, X. F. Jiang, M. Mitome, D. Golberg and Y. Bando, *Nat. Commun.*, 2013, **4**, 2905.
6 M. F. El-Kady, V. Strong, S. Dubin and R. B. Kaner, *Science*, 2012, **335**, 1326–1330.
7 F. Schwierz, *Proc. IEEE.*, 2013, **101**, 1567–1584.

Open Access Article. Published on 23 June 2020. Downloaded on 1/23/2026 11:39:11 PM.
This article is licensed under a Creative Commons Attribution-NonCommercial 3.0 Unported Licence.

8 Y. L. Liu, X. J. Wu, Y. Zhao, X. C. Zeng and J. L. Yang, *J. Phys. Chem. C*, 2011, **115**, 9442–9450.
9 I. Y. Jeon, S. Zhang, L. P. Zhang, H. J. Choi, J. M. Seo, Z. H. Xia, L. M. Dai and J. B. Baek, *Adv. Mater.*, 2013, **25**, 6138–6145.
10 L. Q. Tao, H. Tian, Y. Liu, Z. Y. Ju, Y. Pang, Y. Q. Chen, D. Y. Wang, X. G. Tian, J. C. Yan, N. Q. Deng, Y. Yang and T. L. Ren, *Nat. Commun.*, 2017, **8**, 14579.
11 W. X. Song, J. X. Zhu, B. H. Gan, X. Y. Zhao, H. Wang, C. J. Li and J. Wang, *Small*, 2017, **14**, 1702249.
12 H. L. Poh, P. Šimek, Z. Sofer and M. Pumera, *ACS Nano*, 2013, **7**, 5262–5272.
13 D. Higgins, M. A. Hoque, M. H. Seo, R. Y. Wang, F. Hassan, J. Y. Choi, M. Pritzker, A. Yu, J. J. Zhang and Z. W. Chen, *Adv. Funct. Mater.*, 2014, **24**, 4325–4336.
14 Z. J. Ma, S. Dou, A. Shen, L. Tao, P. L. Dai and P. S. Wang, *Angew. Chem., Int. Ed.*, 2015, **54**, 1888–1892.
15 P. P. Zhang, J. Li, L. X. Lv, Y. Zhao and L. T. Qu, *ACS Nano*, 2017, **11**, 5087–5093.
16 R. S. Steinberg, M. Cruz, N. G. A. Mahfouz, Y. Qiu and R. H. Hurt, *ACS Nano*, 2017, **11**, 5670–5679.
17 W. Li, J. Liu and D. Y. Zhao, *Nat. Rev. Mater.*, 2016, **16**, 16023.
18 F. Bonaccorso, L. G. Colombo, G. H. Yu, M. Stoller, V. Tozzini, A. C. Ferrari, R. S. Ruoff and V. Pellegrini, *Science*, 2015, **347**, 1246501.
19 F. C. Wang, K. D. Wang, B. X. Zheng, X. Dong, X. S. Mei, J. Lv, W. Q. Duan and W. J. Wang, *Materials Technology*, 2018, **33**, 340–356.
20 H. J. Qiu, L. Y. Chen, Y. Ito, J. L. Kang, X. W. Guo, P. Liu, H. Kashani, A. Hirata, T. Fujita and M. W. Chen, *Nanoscale*, 2016, **8**, 18551–18557.
21 H. J. Qiu, P. Du, K. L. Hu, J. J. Gao, H. L. Li, P. Liu, T. Ina, K. Ohara, Y. Ito and M. W. Chen, *Adv. Mater.*, 2019, **31**, 1900843.
22 B. C. Qiu, M. Y. Xing and J. L. Zhang, *J. Am. Chem. Soc.*, 2014, **136**, 5852–5855.
23 J. J. Duan, S. Chen, M. Jaroniec and S. Z. Qiao, *ACS Catal.*, 2015, **5**, 5207–5234.
24 M. F. El-Kady, V. Strong, S. Dubin and R. B. Kane, *Science*, 2012, **335**, 1326–1330.
25 J. Lin, Z. W. Peng, Y. Y. Liu, F. Ruiz-Zepeda, R. Q. Ye, E. L. G. Samuel, M. J. Yacaman, B. I. Yakobson and J. M. Tour, *Nat. Commun.*, 2014, **5**, 5714.
26 F. Zhang, E. Alhajji, Y. J. Lei, N. Kurra and H. N. Alshareef, *Adv. Energy Mater.*, 2018, **8**, 1800353.
27 Y. Dong, S. C. Rismiller and J. Lin, *Carbon*, 2016, **104**, 47–55.
28 R. Q. Ye, Z. W. Peng, T. Wang, Y. N. Xu, J. B. Zhang, Y. L. Li, L. G. Nilewski, J. Lin and J. Tour, *ACS Nano*, 2015, **9**, 9244–9251.
29 L. Guo, Y. L. Zhang, D. D. Han, H. B. Jiang, D. Wang, X. B. Li, H. Xia, J. Feng, Q. D. Chen and H. B. Sun, *Adv. Opt. Mater.*, 2014, **2**, 120–125.
30 F. C. Wang, X. Dong, K. D. Wang, W. Q. Duan, M. Gao, Z. Y. Zhai, C. G. Zhu and W. J. Wang, *Carbon*, 2019, **150**, 396–407.
31 Q. Li, N. Mahmood, J. H. Zhu, Y. L. Hou and S. H. Sun, *Nanotoday*, 2014, **9**, 668–683.
32 G. Xu, B. Ding, J. Pan, J. Han, P. Nie, Y. Zhu, Q. Sheng and H. Dou, *J. Mater. Chem. A*, 2015, **3**, 23268–23273.
33 N. Yang, X. Q. Zheng, L. Li, J. Li and Z. D. Wei, *J. Phys. Chem. C*, 2017, **121**, 19321–19328.
34 R. Ye, Y. Chyan, J. B. Zhang, Y. L. Li, X. Han, C. Kittrell and J. M. Tour, *Adv. Mater.*, 2017, **29**, 1702211.
35 X. H. Cao, Y. M. Shi, W. H. Shi, G. Lu, X. Huang, Q. Y. Yan, Q. C. Zhang and H. Zhang, *Small*, 2011, **7**, 3163–3168.
36 W. F. Chen, S. R. Li, C. H. Chen and L. F. Yan, *Adv. Mater.*, 2011, **23**, 5679–5683.
37 M. A. Worsley, P. J. Pauzauskie, T. Y. Olson, J. Biener, J. H. Satcher and T. F. Baumann, *J. Am. Chem. Soc.*, 2010, **132**, 14067–14069.
38 L. G. Cancado, *Appl. Phys. Lett.*, 2006, **88**, 163106.
39 J. Liu, X. Ren and X. Kang, *Inorg. Chem. Front.*, 2019, **24**, 2082–2089.
40 Y. W. Zhu, *Science*, 2011, **332**, 1537–1541.
41 G. Montaudo, C. Puglisi and E. Scamporrino, *Macromolecules*, 1984, **17**, 1605–1614.
42 L. Z. Zhi, J. Qing and E. Z. Nai, *Polym. Degrad. Stab.*, 2018, **150**, 73–85.
43 Y. Chyan, R. Q. Ye, Y. L. Li, S. P. Singh, C. J. Arnusch and J. M. Tour, *ACS Nano*, 2018, **12**, 2176–2183.
44 R. Srinivasan and W. J. Leigh, *J. Am. Chem. Soc.*, 1982, **104**, 6784–6785.
45 H. Schmidt, J. Ihlemann, B. Wolff-Rottke, K. Luther and J. Troe, *J. Appl. Phys.*, 1998, **83**, 5458–5468.
46 Z. S. Wu, K. Parvez, X. L. Feng and K. Mullen, *Nat. Commun.*, 2013, **4**, 2487.
47 M. Beidaghi and C. L. Wang, *Adv. Funct. Mater.*, 2012, **22**, 4501–4510.

 This journal is © The Royal Society of Chemistry 2020